J. Fluid Mech. (2008), *vol.* 598, *pp.* 177–199.
doi:10.1017/S0022112007000122 Printed in the United Kingdom

Direct numerical simulations of rotating turbulent channel flow

OLOF GRUNDESTAM[1], STEFAN WALLIN[1,2] AND ARNE V. JOHANSSON[1]

[1]Linné Flow Center, KTH Mechanics, SE-100 44 Stockholm, Sweden

[2]Computational Physics, Swedish Defence Research Agency (FOI), SE-164 90 Stockholm, Sweden

(Received 30 June 2006 and in revised form 23 November 2007)

Fully developed rotating turbulent channel flow has been studied, through direct numerical simulations, for the complete range of rotation numbers for which the flow is turbulent. The present investigation suggests that complete flow laminarization occurs at a rotation number $Ro = 2\Omega\delta/U_b \leqslant 3.0$, where Ω denotes the system rotation, U_b is the mean bulk velocity and δ is the half-width of the channel. Simulations were performed for ten different rotation numbers in the range 0.98 to 2.49 and complemented with earlier simulations (done in our group) for lower values of Ro. The friction Reynolds number $Re_\tau = u_\tau\delta/\nu$ (where u_τ is the wall-shear velocity and ν is the kinematic viscosity) was chosen as 180 for these simulations. A striking feature of rotating channel flow is the division into a turbulent (unstable) and an almost laminarized (stable) side. The relatively distinct interface between these two regions was found to be maintained by a balance where negative turbulence production plays an important role. The maximum difference in wall-shear stress between the two sides was found to occur for a rotation number of about 0.5. The bulk flow was found to monotonically increase with increasing rotation number and reach a value (for $Re_\tau = 180$) at the laminar limit ($Ro = 3.0$) four times that of the non-rotating case.

1. Introduction

Rotating turbulent channel flow represents a generic flow situation where the intriguing effects of rotation on turbulence can be visualized in a systematic manner. For spanwise rotations, the mean Coriolis force is proportional to the magnitude of the velocity and is oriented in the wall-normal direction. Hence, the magnitude of the Coriolis force increases with increasing distance from the wall, and on the side where the Coriolis force points towards the wall we have the equivalent of an unstable density stratification. In this region, the fluid elements will tend to move and thereby increase wall-normal mixing. This side is referred to as the unstable side. On the other side (the stable side) there is the equivalent of a stable density stratification and turbulence will there be suppressed.

The two layers, one with a strong tendency towards laminarization and one with intensified mixing and rotation-induced structures, co-exist side by side and interact. This gives a situation that forms a prediction challenge for both RANS- (Reynolds-averaged Navier–Stokes) based turbulence models and large-eddy simulations (LES).

The development of a linear mean velocity profile in the centre of the channel where the slope is close to twice the angular rotation rate is a striking feature of this flow.

Of central interest for the understanding of rotational effects on turbulent flows and their prediction is the study of the variation with angular rotation rate of the many rotation-induced features.

The geometry of the flow case is the simplest possible, with two parallel infinite walls with fluid in between that is driven by a pressure gradient. The simplicity of the case makes it suitable for numerical as well as experimental investigations. An experimental set-up must be long and wide enough so that the in- and outflow conditions as well as the sidewalls have a negligible effect on the developed flow. In direct numerical simulations (DNS) periodic boundary conditions are used in the stream- and spanwise directions in order to obtain 'infiniteness'. It is, however, crucial to have a computational domain (or box) that is large enough to contain the largest flow structures in order to minimize the effects of the periodic boundary conditions.

Previous works include the study by Kim, Moin & Moser (1987) who investigated non-rotating channel flow at $Re_\tau = 180$. A domain size of $4\pi\delta \times 2\delta \times 2\pi\delta$ in the streamwise, wall-normal and spanwise directions respectively, was used in combination with a pseudo-spectral method on a $192 \times 129 \times 160$ grid. Many other studies of non-rotating channel flow have followed in recent years.

Rotating channel flow has been studied through DNS by for instance Kristoffersen & Andersson (1993). The size of the computational domain was the same as that of Kim *et al.* (1987) but with a Reynolds number slightly larger (i.e. $Re_\tau = 194$). Second-order central differences for the spatial derivatives in combination with a resolution of $128 \times 128 \times 128$ were used. Lamballais, Lesieur & Métais (1996) considered both transitional and turbulent channel flow subject to rotation. The box length in the periodic directions was reduced by a factor 2 compared to Kristoffersen & Andersson (1993). Lamballais, Métais & Lesieur (1998) performed an LES study of rotating and non-rotating channel flow. Experimental studies of rotating channel flow have been performed by e.g. Johnston, Halleen & Lezius (1972), Nakabayashi & Kitoh (1996, 2005) and Maciel *et al.* (2003).

Alvelius (1999) performed simulations of turbulent rotating channel flow for $Re_\tau = 180$ and 360. A computational domain as large as $8\pi\delta \times 2\delta \times 3\pi\delta$ was used in some of the simulations. It was concluded that even though the box was very large it was too short to completely capture the very elongated structures occurring at the lowest rotation numbers. The box-length requirement was, however, found to be less strict for higher rotation numbers.

Oberlack (2001) studied a group of flows through the use of symmetry methods and deduced specifically for rotating channel flow that the applied system rotation breaks the time-scaling symmetry in the centre of the channel. As a result, the slope of the mean velocity profile in this region should be proportional to the system rotation rate. However, the proportionality constant is left as a free parameter with this procedure and Oberlack (2001) refers to experimental and DNS studies regarding this.

Wu & Kasagi (2004) performed an investigation of turbulent channel flow subject to arbitrary system rotation by using combinations of streamwise, spanwise and wall-normal rotation rates. By combining two orthogonal rotations, three different families of cases were studied. Wu & Kasagi (2004) concluded that the spanwise rotation, if applied, has the dominating effect on the flow. Nagano & Hatori (2003) used the classical spanwise system rotation but also included heat transfer in their study.

The present study complements an earlier investigation in our group, by Alvelius (1999), with new simulations for higher rotation numbers for the case of turbulent channel flow rotating around the spanwise axis. The aim is to investigate the whole range of rotation numbers for which the flow is turbulent and eventually to determine

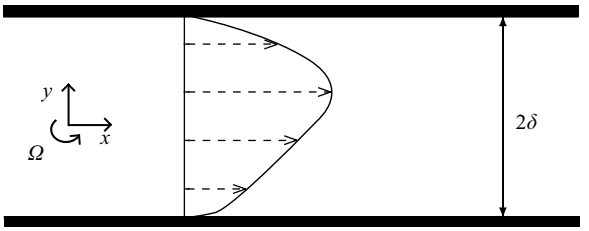

FIGURE 1. A schematic of the geometry and mean flow.

for which rotation number the flow laminarizes, or alternatively, to investigate what happens for high rotation numbers. The present study makes use of the combined database for the simulations in order to cover a wide range of the rotation numbers. This allowed us to study trends of the behaviour of flow structures and statistical features. Of special interest is the behaviour of the wall-shear velocity on the different sides of the channel. Alvelius (1999) predicted that the difference between the wall-shear velocity on the stable and unstable sides should decrease with increasing rotation number for sufficiently high rotation numbers. This trend is in contrast to that for low rotation numbers and is verified in this paper.

2. Flow case description and equations

The fundamental characteristics of the present flow case are well known and have been given previously by numerous authors, see e.g. Kristoffersen & Andersson (1993) and Lamballais *et al.* (1996). A description will also be given here for completeness. A schematic picture of the flow is shown in figure 1. A pressure gradient is applied in the x-direction in order to drive the flow. In the coordinate system shown in the figure, the rotation is applied in the positive z-direction. The channel half-width is denoted δ and the velocities in the x, y and z-directions are denoted u, v and w respectively. Alternatively, the coordinates and velocities are denoted x_i and u_i with $i = 1, 2, 3$. When studying the flow field, the instantaneous velocity and pressure fields can be decomposed into a mean and fluctuating part as $u_i = U_i + u_i'$ and $p = P + p'$, where $U_i = \overline{u}_i$ and $P = \overline{p}$ and a bar means averaging of a quantity. In the present study the averaging is in the homogeneous directions by combining typically fifteen to twenty fields well separated in time and thus statistically independent.

When rotation is applied in the spanwise direction ($\Omega_i = \Omega\delta_{i3}$), the previously symmetric mean velocity profile becomes asymmetric and the channel is divided into a pressure (unstable) and suction (stable) side. The wall-shear velocity, defined as

$$u_\tau = \sqrt{\nu \left| \frac{\mathrm{d}U}{\mathrm{d}y} \right|_{\mathrm{wall}}} \tag{2.1}$$

for non-rotating channel flow, is affected by this and for the rotating case is given by

$$u_\tau = \sqrt{u_\tau^{u2}/2 + u_\tau^{s2}/2} \tag{2.2}$$

where u_τ^u and u_τ^s are the wall-shear velocities on the unstable and stable sides, respectively. Correspondingly, there are Reynolds numbers associated with these velocities, Re_τ^u and Re_τ^s, besides Re_τ which is defined as

$$Re_\tau = \frac{u_\tau \delta}{\nu}. \tag{2.3}$$

It is also useful to define a Reynolds number based on the mean bulk velocity, U_b, as

$$Re_b = \frac{U_b \delta}{\nu} \tag{2.4}$$

where U_b is obtained through

$$U_b = \frac{1}{2\delta} \int_{-\delta}^{+\delta} U(y)\, \mathrm{d}y. \tag{2.5}$$

Many previous studies, see e.g. Kristoffersen & Andersson (1993), Lamballais *et al.* (1996) and Alvelius (1999), indicate that $\mathrm{d}U/\mathrm{d}y$ is very close to 2Ω in the centre of the channel. As a result, an increased rotation rate gives an increased mean bulk flow. This implies that the rotation number based on the mean bulk velocity, U_b, defined as

$$Ro = \frac{2\Omega\delta}{U_b}, \tag{2.6}$$

increases at a rate that is considerably slower than proportional to the rotation rate. Alternatively, a rotation number based on u_τ can be defined as $Ro^+ = 2\Omega\delta/u_\tau$. Note that Ro^+ is directly proportional to the system rotation rate since u_τ is constant for constant-pressure-gradient channel flow.

2.1. *Governing equations*

All details of rotating turbulent channel flow are governed by the incompressible Navier–Stokes equations formulated in a rotating frame of reference which, together with the continuity condition, are given by

$$\frac{\partial u_i}{\partial t} + u_j \frac{\partial u_i}{\partial x_j} = -\frac{1}{\rho}\frac{\partial p}{\partial x_i} + \nu \frac{\partial^2 u_i}{\partial x_j \partial x_j} + 2\epsilon_{ijk} u_j \Omega_k, \tag{2.7}$$

$$\frac{\partial u_i}{\partial x_i} = 0. \tag{2.8}$$

In the present study where only spanwise rotation is considered, the components of the rotation vector are given by $\Omega_i = \Omega\delta_{i3}$. The centrifugal acceleration term is absorbed into the pressure and the last term of (2.7) represents the Coriolis force. As discussed at the beginning of § 1, the mean Coriolis force is directly proportional to the streamwise mean velocity, U. This implies that the region of unstable stratification will extend from the wall on the unstable side to the point where $\mathrm{d}U/\mathrm{d}y = 0$. Correspondingly, the stable stratification is restricted to the part of the channel where $\mathrm{d}U/\mathrm{d}y < 0$. It should be noted that in some previous studies, the stable and unstable side have been denoted the suction and pressure side, respectively.

Fundamentally important characteristics of channel flow can be understood by investigating the equations for the mean velocity, the Reynolds-averaged Navier–Stokes (RANS) equations. These equations are obtained by averaging over time or the homogeneous spatial directions. For a fully developed channel flow only the x-component of the mean velocity is non-zero. Hence, the RANS equations reduce to

$$0 = -\frac{1}{\rho}\frac{\partial P}{\partial x} + \frac{\mathrm{d}}{\mathrm{d}y}\left(\nu \frac{\mathrm{d}U}{\mathrm{d}y} - \overline{u'v'}\right). \tag{2.9}$$

Worth noting here is that the effect of system rotation on the mean flow enters only through the $\overline{u'v'}$-component of the Reynolds stress tensor since the corresponding mean Coriolis term has zero x-component. Since $\mathrm{d}^2U/\mathrm{d}y^2$ is negative, the slope of

$\overline{u'v'}$ cannot be larger than $-(\partial P/\partial x)/\rho$. In the centre of the channel, away from the wall where $\nu \mathrm{d}^2U/\mathrm{d}y^2$ is very small, the slope of $\overline{uv}$ can therefore be *approximated* by $-(\partial P/\partial x)/\rho$ and is thus essentially independent of the rotation rate for a given imposed pressure gradient. By integrating across the channel from the wall, y_w, to some position y, one can further deduce that the total shear is given by the expression

$$\nu \frac{\mathrm{d}U}{\mathrm{d}y} - \overline{u'v'} = \nu \frac{\mathrm{d}U}{\mathrm{d}y}\bigg|_{y=y_w} + \frac{1}{\rho}\frac{\partial P}{\partial x}(y - y_w). \tag{2.10}$$

From this it is obvious that the wall-shear velocity is related to the pressure gradient by $\partial P/\partial x = -(\rho/\delta)u_\tau^2$. This also holds in the rotating cases when u_τ is the total wall-shear velocity defined by (2.2). Note that for the rotating case, the value of the term $\nu(\mathrm{d}U/\mathrm{d}y)|_{y=y_w}$ in (2.10) will depend on whether the integration is done from the stable or unstable side of the channel. This results in an offset in the y-direction of the total shear for the rotating case compared to the non-rotating case.

The effect of rotation enters through the equation for the Reynolds stresses

$$\frac{\partial \overline{u_i'u_j'}}{\partial t} + U_k \frac{\partial \overline{u_i'u_j'}}{\partial x_k} = \mathscr{P}_{ij} + \Pi_{ij} - \varepsilon_{ij} + \mathscr{D}_{ij} + C_{ij} \tag{2.11}$$

through the Coriolis term given by

$$C_{ij} = -2\Omega_k(\overline{u_i'u_m'}\epsilon_{mjk} - \varepsilon_{imk}\overline{u_m'u_j'}). \tag{2.12}$$

The remaining terms in (2.11) represent production, dissipation, pressure–strain and diffusion, respectively, and are defined as

$$\mathscr{P}_{ij} = -\overline{u_i'u_m'}\frac{\partial U_j}{\partial x_m} - \overline{u_j'u_m'}\frac{\partial U_i}{\partial x_m}, \tag{2.13}$$

$$\varepsilon_{ij} = 2\nu\overline{u_{i,m}'u_{j,m}'}, \tag{2.14}$$

$$\Pi_{ij} = \frac{2}{\rho}\overline{p's_{ij}'}, \tag{2.15}$$

$$\mathscr{D}_{ij} = -T_{ij} - G_{ij} + D_{ij}^{\nu}, \tag{2.16}$$

where the different parts of the diffusion are given by

$$T_{ij} = \frac{\partial}{\partial x_m}\overline{u_i'u_j'u_m'}, \tag{2.17}$$

$$G_{ij} = \frac{\partial}{\partial x_m}\left(\frac{1}{\rho}(\overline{u_j'p'}\delta_{im} + \overline{u_i'p'}\delta_{jm})\right), \tag{2.18}$$

$$\mathscr{D}_{ij}^{\nu} = \frac{\partial}{\partial x_m}\left(\nu\frac{\partial \overline{u_i'u_j'}}{\partial x_m}\right). \tag{2.19}$$

From a turbulence modelling perspective the production and the Coriolis terms are the only terms that can be expressed exactly as combinations of the known quantities (those that are solved for). The rest, i.e. the pressure–strain, dissipation and diffusion, must be modelled. Therefore, DNS provides the modeller with a useful tool for investigating the properties of the different components of a turbulence model. By evaluating the correlations that normally need to be modelled, the turbulence model developer can make so-called *a priori* tests and compare the actual model predictions with the exact expression for a given mean flow and Reynolds stress statistics. In this way, the physical correctness of each of the terms can be studied rather than the

model performance as a whole. Part of the aim of the present study is to provide flow data in order to be able to develop a database for *a priori* testing.

2.2. *Plausible scenarios for high Ro*

Before considering the simulations for high Ro, it may be useful to consider the plausible flow scenarios in this parameter region. First, one can conclude that all previous studies of rotating turbulent channel flow have shown that the slope of the mean velocity profile is very close to 2Ω in a part of the domain. In the previous studies by e.g. Kristoffersen & Andersson (1993) and Alvelius (1999) this behaviour has been shown to give an increasing mean bulk velocity with increasing rotation number if a constant pressure gradient is applied. It is plausible that this trend is broken at some point before or when the bulk flow would exceed that of the corresponding laminar flow and that the flow is completely laminarized at this point. Based on observations from earlier studies for lower rotation numbers, it seems sound to assume that there is a region of the channel in which the mean velocity profile has a slope of 2Ω as long as the flow is turbulent. It is also reasonable to assume that the bulk velocity never exceeds the velocity of the corresponding laminar flow. These two assumptions then imply that, for high Ro, the 2Ω-slope region can only extend over a part of the domain on the unstable side where the corresponding laminar velocity profile has a slope larger than 2Ω. For increasing Ω, the 2Ω-region should hence decrease in extent until 2Ω is equal to the slope of the laminar velocity profile at the wall. At this point, the 2Ω-region is 'infinitely thin' and the flow is laminar. In this scenario the transition from turbulent to laminar flow is smooth and continuous with respect to Ω. It should be noted that, for rotating Couette flow, Bech & Andersson (1997) discovered that complete laminarization occurs when 2Ω equals the slope of the laminar velocity profile. This is the direct analogue to when 2Ω is equal to the slope of the laminar velocity profile at the wall for rotating channel flow.

The rotation number for which the laminarization occurs can be deduced by considering the slope of the laminar velocity profile at the wall, $\mathrm{d}U_w^{lam}/\mathrm{d}y$, and the corresponding bulk velocity, U_b^{lam}. One must then have that $2\Omega = \mathrm{d}U_w^{lam}/\mathrm{d}y$ which gives $Ro = \delta(\mathrm{d}U_w^{lam}/\mathrm{d}y)/U_b^{lam}$. By simply evaluating $\mathrm{d}U_w^{lam}/\mathrm{d}y$ and U_b^{lam} for the laminar flow it is easily seen that laminarization would occur at $Ro = 3.0$. The present study, as will be shown below, indicates that this scenario holds and that the flow is laminarized at $Ro = 3.0$ and, furthermore, that a 2Ω-slope region is present as long as the flow is turbulent.

A study incorporating a very high rotation number was performed by Lamballais *et al.* (1996). In their investigation, transitional flow at rotation number 30.0 was considered. The initial random perturbations of small amplitude, imposed on the laminar velocity profile, developed into nonlinear saturated two-dimensional Tollmien–Schlichting waves. Lesieur, Métais & Comte (2005) further discuss important aspects of the flow physics for different rotation numbers.

3. Simulations

The pseudo-spectral code by Lundblad, Henningson & Johansson (1992) was used in the present study. It is based on the velocity–vorticity formulation and solves for the wall-normal vorticity, ω_2, and the Laplacian of the wall-normal velocity, Δu_2. In this way, the fluctuating pressure is eliminated from the equations. Fourier series expansions are used in the periodic x- and z-directions together with Chebyshev series in the y-direction. Fast Fourier transforms (FFT) are used in the transformation

Ro	Ro^+	Re_τ^s	Re_τ^u	Re_b	n_y
0.98	22.0	138.4	213.9	4026	129
1.07	25.6	141.1	212.1	4313	129
1.15	29.4	143.7	209.7	4601	129
1.21	33.1	146.5	207.4	4904	129
1.27	36.9	148.8	206.3	5193	161
1.50	55.0	159.1	198.6	6592	161
1.69	73.3	166.3	193.0	7809	161
1.87	91.7	171.3	188.4	8810	201
2.06	110.0	174.9	185.0	9605	201
2.49	146.7	179.2	180.8	10 597	201
3.00	180.0	180.0	180.0	10 800	201

TABLE 1. Rotation and Reynolds numbers. The n_y-column shows number of nodes in wall-normal direction.

between Fourier and physical space. Time integration is done using a Crank–Nicholson scheme for the linear terms and a four-stage Runge–Kutta method for the nonlinear terms. The flow is driven by a prescribed constant pressure gradient. In this way the value of u_τ and hence also Re_τ and $l^* = \nu/u_\tau$ are given for the fully developed flow.

Simulations of fully developed rotating channel flow have been performed for $Re_\tau = 180$ with the rotation numbers ranging from $Ro = 0.98$ to 2.49, corresponding to $Ro^+ = 2\delta\Omega/u_\tau = 22.0$ to 146.7. The simulation for a particular Ro was initialized with a velocity field from the preceding simulation of lower rotation number. The first simulation was initialized with a velocity field in which lower wavenumbers had been excited in such a way that continuity was fulfilled.

For brevity, we have chosen to focus on $Ro = 0.98$, 1.50, 2.06 and 2.49. The size of the computational domain was $4\pi\delta \times 2\delta \times 2\pi\delta$. An increase, with increasing Ro, in wall-normal resolution from 129 to 161 to 201 modes was necessary in order to obtain a numerically converged solution (see table 1 for details regarding rotation number, wall-normal resolution, etc). For $Re_\tau = 180$ this corresponds to a node spacing of $\Delta x^+ = 11.8$ and $\Delta z^+ = 7.1$ in the stream- and spanwise directions, respectively, and an average node spacing in the y-direction of $\Delta y^+ = 2.8$, 2.23 and 1.79 for the three different wall-normal resolutions, respectively.

Numerous investigations of channel flow, using DNS, have been reported during recent years. The demands on spatial resolution set by numerical accuracy requirements have been studied and the values used in the present study fall in the range used in well-resolved simulations of non-rotating channel flow.

In order to obtain an indication of the expected flow laminarization at $Ro = 3.0$ an initial field consisting of a laminar velocity distribution with superimposed disturbances of the type proposed by Henningson, Lundbladh & Johansson (1993) was created. These disturbances consist of streamwise counter-rotating vortices and are shown in figure 2 in which contours of the wall-normal velocity are displayed. The disturbance amplitude corresponds to 1.0% of the maximum value of the streamwise (laminar) velocity. The system rotation rate was set in accordance with $Ro = 3.0$ for a laminar flow. These velocity disturbances decayed.

The computations were carried out on the Lenngren and Lucidor clusters at Parallelldatorcentrum (PDC), KTH. The simulations were performed using up to 40 processors.

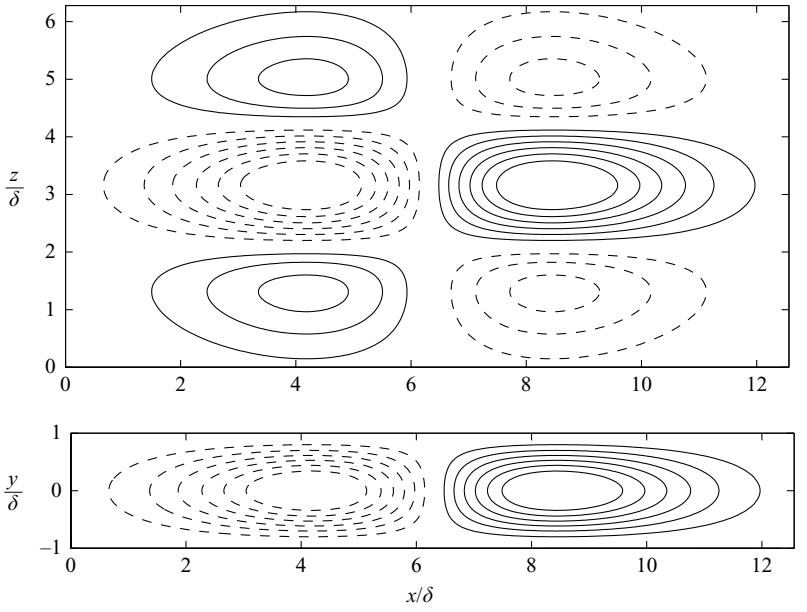

FIGURE 2. Initial wall-normal velocity, contour spacing 0.05^+ (wall units): (*a*) at $y/\delta = 0$, (*b*) at $z/\delta = 3.14$.

4. Structures

In order to minimize the effect of the periodic boundary conditions it is important to have a computational box large enough to contain the largest structures of the flow. The size of the flow structures can be estimated through the two-point correlation defined as

$$tp[f](y, \boldsymbol{r}) = \frac{\overline{f'(\boldsymbol{x}+\boldsymbol{r})f'(\boldsymbol{x})}}{\overline{(f')^2}}. \tag{4.1}$$

If the box is sufficiently large, the two-point correlation is small at distances of half the box size in the direction considered.

The two-point correlations of the streamwise fluctuating velocity, u', as functions of y are shown in figure 3 for four different rotation numbers between 0.98 and 2.49 and streamwise separations of up to half the box length in the x-direction. On the unstable side of the channel the correlations are small for all rotation numbers. The correlation lengths on the stable side are, on the other hand, significantly larger. For some of the rotation numbers, a periodicity in the x-direction can be observed close to the wall on the stable side of the channel. This is related to the elongated flow structures in this region and is further discussed below. Differences in the two-point correlation of u', for low and intermediate rotation numbers, between the pressure and suction side have previously been discussed by e.g. Kristoffersen & Andersson (1993) and Alvelius (1999). Their results indicate that the largest correlations are attained at low rotation rates for which long structures are formed on the stable side of the channel while the turbulence levels are still of the same order as for the non-rotating case. Lamballais *et al.* (1998) consider arbitrary separations and show isosurfaces for the two-point correlations of the streamwise velocity fluctuations and vorticity on the unstable side of the channel. Their results indicate that the streamwise

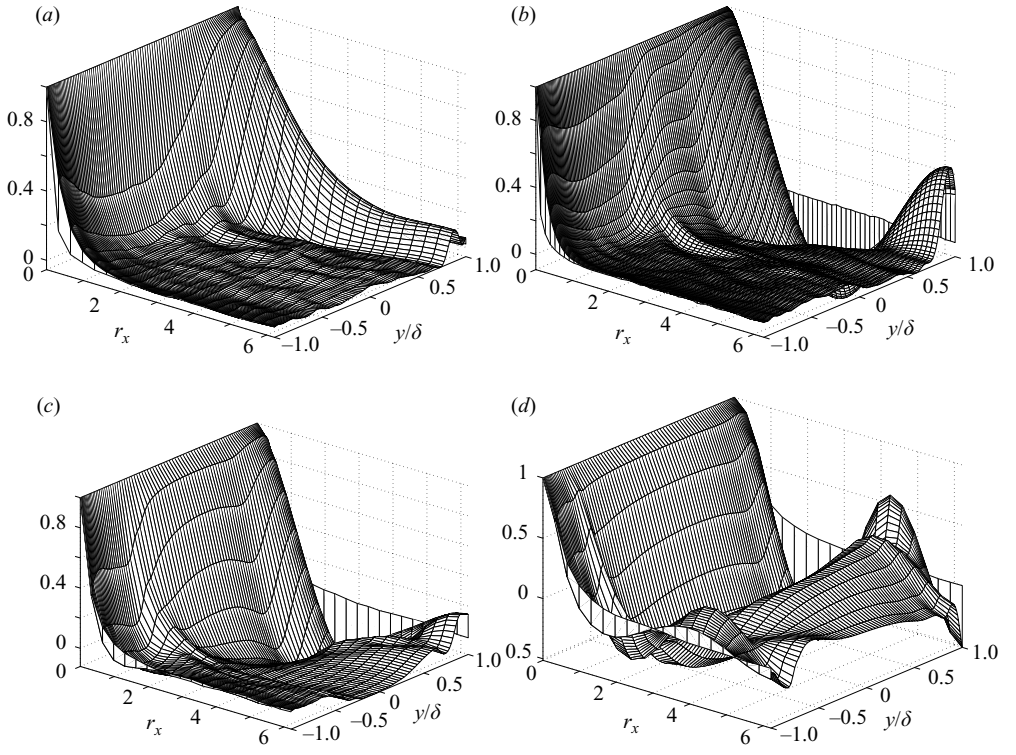

FIGURE 3. Two-point correlation of u', $tp[u'](y, r_x)$, as function of y and separation r_x in the x-direction for: $Re_\tau = 180$, and (*a*) $Ro = 0.98$, (*b*) 1.50, (*c*) 2.06 and (*d*) 2.49.

correlation length of u' close to the wall on the unstable side is shorter for $Ro = 1.50$ than for the non-rotating case.

With respect to the high correlations seen on the stable side of the channel for large separations for some rotation numbers, it is not possible to exclude an influence of the periodic boundary conditions on the flow. However, as is demonstrated below in § 5.2, the turbulence levels are very low in the part of the domain where $tp[u']$ attains its largest value. It should also be noted that the maximum value of $tp[u']$ on the stable side is located much closer to the wall than the peak of the $\overline{u'u'}^+$-profile. These residues of turbulence mainly consist of large structures of low intensity and will be present until the flow is completely laminarized. Hence, whereas the correlations are high close to the wall on the stable side of the channel, the low turbulence intensities imply that any physical inconsistences occurring in this region due to periodic boundary conditions should be of minor importance.

In figures 4 to 6 various contour and magnitude plots are shown for the instantaneous streamwise and wall-normal fluctuating velocities at different, rotation numbers. Figures 4 and 5 show (x, y)-planes of instantaneous fluctuating streamwise and wall-normal velocity for $Ro = 0.98$ and $Ro = 2.06$. Relative magnitude differences are indicated by colour. As a complement, velocity contours are imposed in the corresponding plots. The plots of a particular figure correspond to the same instantaneous velocity field and plane. For $Ro = 0.98$ (figure 4), the turbulence is suppressed on the stable side of the channel where there are no small-scale flow structures. The wall-normal velocity fluctuations are restricted to a distinct region on

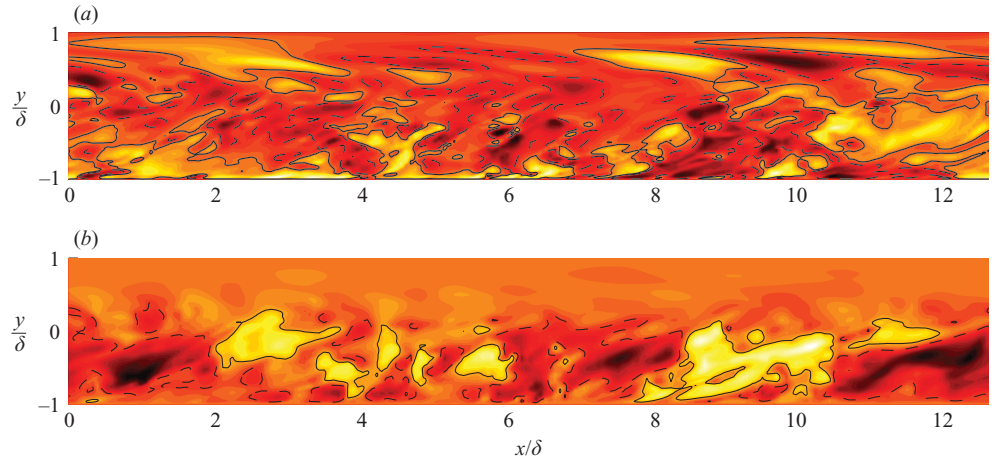

FIGURE 4. Magnitude and contour plots of instantaneous u' (a) and v' (b) for $Ro = 0.98$ in an (x, y)-plane. $u'^{+} = 0.5$ (—) and $u'^{+} = -0.5$ (– –) for the streamwise fluctuating velocity. $v'^{+} = 1.0$ (—) and $v'^{+} = -1.0$ (– –) for the wall-normal fluctuating velocity.

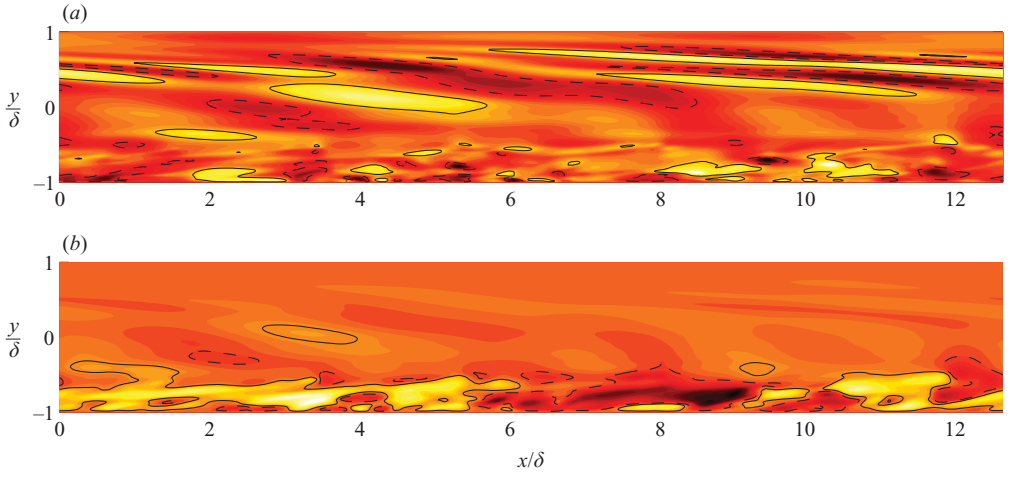

FIGURE 5. As figure 4 but for $Ro = 2.06$.

the unstable side of the channel. The streamwise fluctuating velocity shows the same type of trend but still has the elongated and slanted structures. A small tilting of the structures can also seen as a natural consequence of the action of mean shear.

For $Ro = 2.06$ (figure 5), the turbulence is strongly damped and has significant wall-normal fluctuations ($v'^{+} = \pm 1$) only in a thin band close to the wall on the unstable side. The streamwise fluctuations are significant over a much wider part of the channel, but the characteristics of the stable and unstable sides are still fundamentally different, with small structures on the unstable side and long slightly slanted structures on the stable side. This indicates that the turbulence is strongly stratified in the wall-normal direction, with an active unstable side which influences the passive stable side. Hence, with the aid of these plots we may interpret the large extended u'-structures on the stable side as a response to the 'forcing' of the stable side from the wall-normal fluctuations on the unstable side. The longer slanted structures on the stable side for the higher rotation numbers are reflected in the behaviour of the corresponding

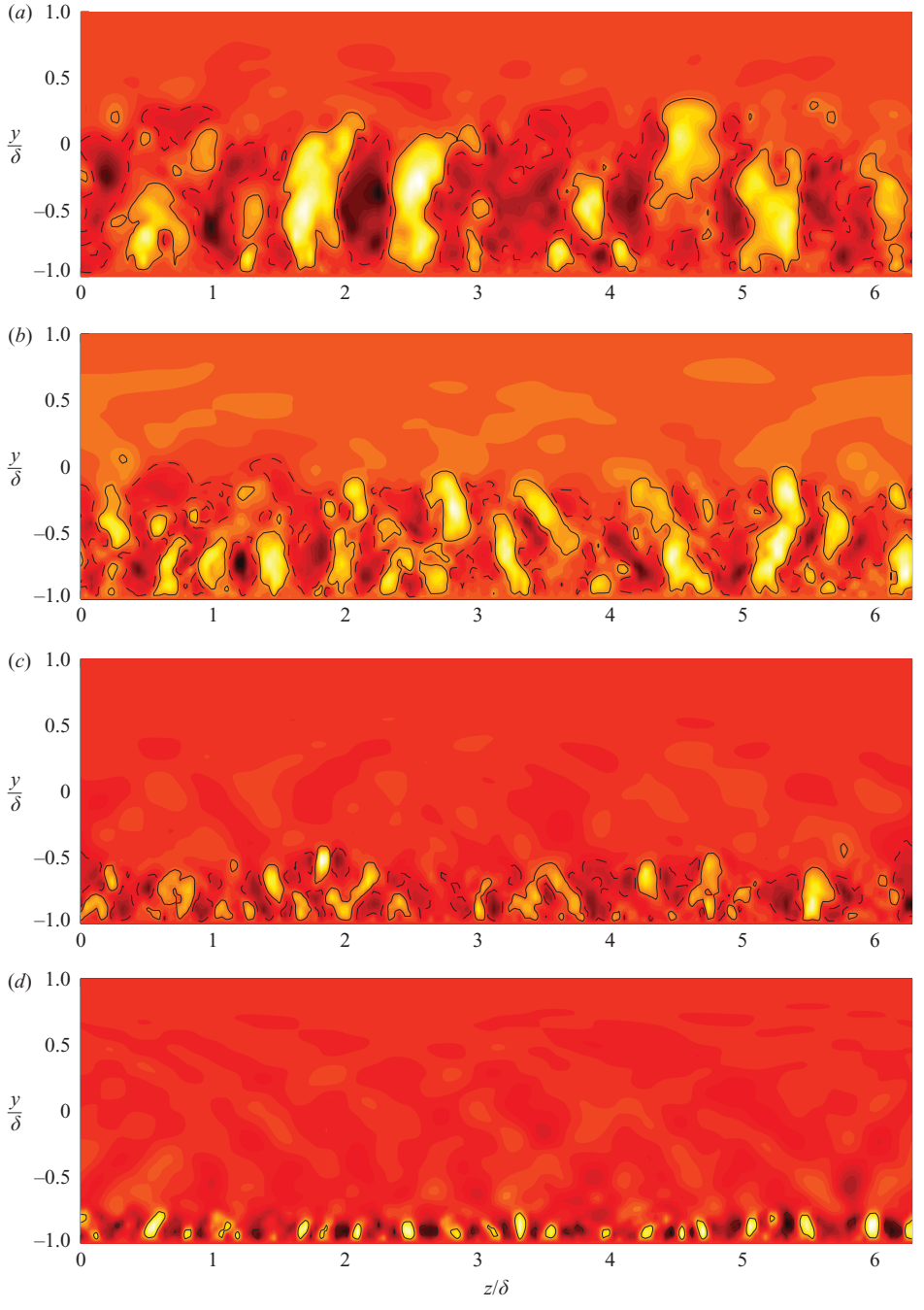

FIGURE 6. Wall-normal velocity fluctuations: magnitude and contour plots of $v'^{+} = 1.0$ (—) and $v'^{+} = -1.0$ (——) in (y, z)-plane for (*a*) $Ro = 0.98$, (*b*) 1.50, (*c*) 2.06 and (*d*) 2.49.

two-point correlations shown in figure 3 in which a periodicity with relatively large correlations can be observed, even for separations up to half the box length in the x-direction.

The strong restriction of the wall-normal velocity fluctuations to an increasingly thin part of the unstable side of the channel, for increasing rotation numbers, seen in figures 4 and 5, is also seen in the (y, z)-planes shown in figure 6. This flow feature is strikingly clear from these plots and should be seen as the underlying mechanism for the increasingly laminar-like flow for increasing rotation rate.

4.1. *Elongated streamwise structures, roll cells*

Elongated streamwise counter-rotating vortices, so-called roll cells, have been observed in previous investigations of rotating turbulent channel flow, see e.g. Johnston *et al.* (1972) and Kristoffersen & Andersson (1993). These roll cells have been shown to be present on the unstable side of the channel for a variety of rotation numbers. Whereas the time-scale of the roll cells is long compared to the turbulence time scale, $\tau = K/\varepsilon$ (where K is the kinetic energy and ε its dissipation rate), a very limited number of simulations indicate a long-time steadiness of this kind of structure. Johnston *et al.* (1972) reported that the time scale of the roll cells was long in comparison to the other turbulence scales, but no truly steady structure of this type was found. In the study by Kristoffersen & Andersson (1993), roll cells with a longer time scale than the total sampling time of $5.6\delta/u_\tau$ were obtained for $Ro = 0.15$. This was, however, the only rotation number in their study for which these structures persisted over the total sampling period. Lamballais *et al.* (1998) also address roll cells and conclude that they are identifiable for small rotation numbers, but that they seem to vanish for higher rotation numbers and become more unstable for high Reynolds numbers. In the present study, the illustration of roll cells has been restricted to one rotation number, $Ro = 1.27$.

This investigation is carried out by studying, cross-stream (y, z) planes. Three cases have been explored: (i) an instantaneous (y, z)-plane, (ii) a (y, z)-plane averaged over a complete computational field (same field as (i)) and (iii) a (y, z)-plane averaged over all fields. The samples used for case (iii) consists of twenty-one different fields equally spaced in time over a total time interval of $\sim 109\delta/u_\tau$. The results for the wall-normal and spanwise velocity components for (i) and (ii) are shown in terms of velocity contours in figure 7. The wall-normal and spanwise velocities for (ii) are denoted $\overline{v}^f$ and $\overline{w}^f$ respectively. When averaged over a single field, the corresponding cross-stream-plane flow pattern shows structures that are similar to roll cells, see figures 7(*b*) and 7(*d*). These patterns are, naturally, somewhat different from those of the instantaneous planes, see figures 7(*a*) and 7(*c*). It is important to note that the area of the cross-sectional plane that has velocity magnitudes larger than those indicated by the contours is smaller when averaged over a complete field than for the instantaneous case. Furthermore, when considering (iii), and hence averaging over all streamwise position of all fields, the magnitude of the averaged wall-normal and spanwise velocity components in no part of the corresponding plane exceeds the value of 0.5 wall units. The plot corresponding to figure 7 would for case (iii) hence be empty, and is therefore not shown. It should be pointed out, however, that even for this case flow patterns similar to those of case (ii) can be seen if the iso-contour value is chosen adequately low. One can observe that the spanwise position of this pattern does not exactly coincide with the pattern of case (ii). This indicates that the observed structures are non-stationary. Furthermore, the decrease in magnitude for increased sampling periods inevitably implies that the averged pattern should vanish when very long sampling periods are used.

Streamwise roll cells can also be identified by two-point correlations in the stream- and spanwise directions. These correlations are plotted for the wall-normal and

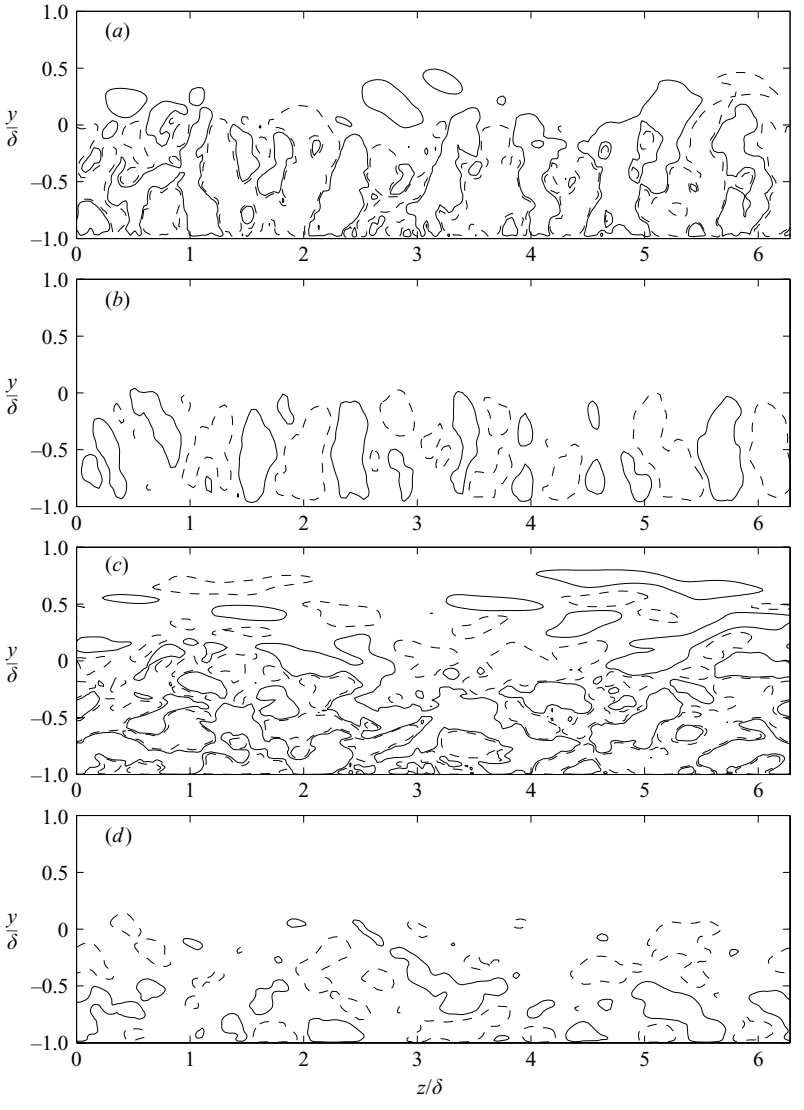

FIGURE 7. Velocity contours in (y, z)-planes at $Ro = 1.27$ for (a) instantaneous $v'^{+} = \pm 0.5$ at one x-position, (b) v' averaged over one field, $\overline{v}^{f+} = \pm 0.5$, (c) instantaneous w' at the same x-position as (a) and (d) w' averaged over one field $\overline{w}^{f+} \pm 0.5$.

spanwise velocities for $Ro = 1.27$ in figure 8. Stationary roll cells, if present, would be seen as significant magnitudes in the two-point correlations of v' and w' on the unstable side of the channel up to large streamwise separations. The same flow structures would give oscillations, with the same period seen in figure 7(a, b), of significant magnitude in the spanwise correlations for large separations in this part of the channel. An example of such behaviour is given by Kristoffersen & Andersson (1993) for $Ro = 0.15$, the rotation number for which the roll cells persisted over the entire sampling period. In the present study, strong negative correlations can be seen for small spanwise separations for both v' and w'. It can be noted that this separation is of the same order as the spanwise extent of the structures discussed above. For larger separations, small oscillations are presented, but the magnitude is very small.

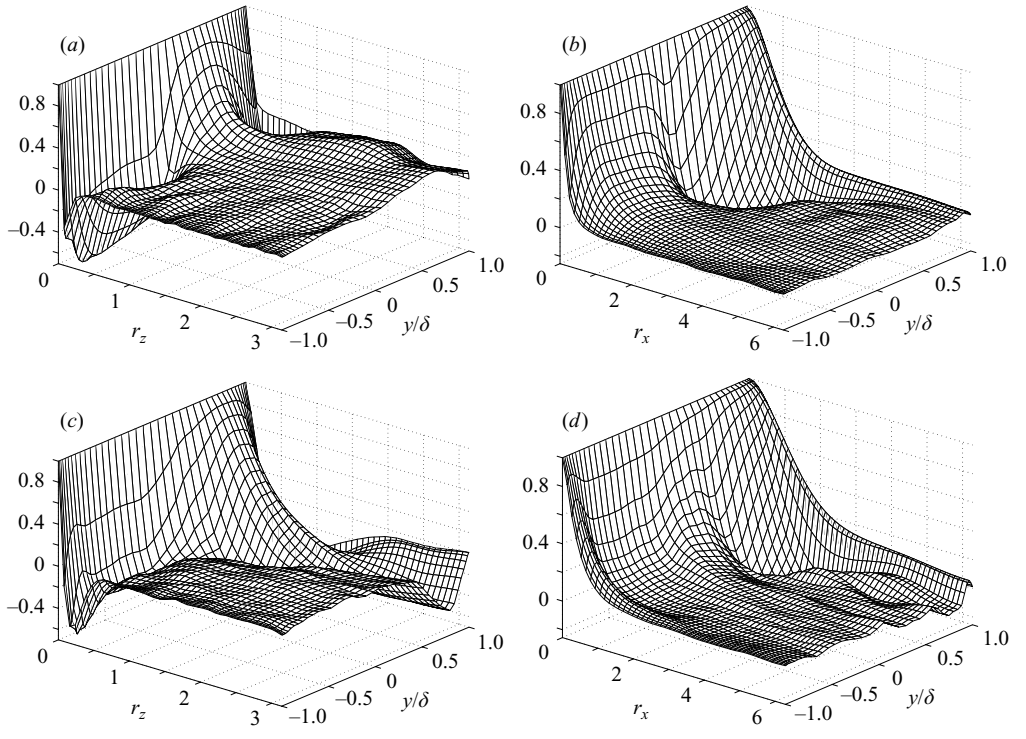

FIGURE 8. Two-point correlation for $Ro = 1.27$ of (a) v' for spanwise separations, (b) v' for streamwise separations, (c) w' for spanwise separations and (d) w' for streamwise separations.

While a strong correlation for short spanwise separations indicates that there are streamwise vortex-like structures, the weak correlation for larger separations means that these vortices are unsteady in space. A shift to negative values of significant magnitude can be observed for w' at $y/\delta \sim 0.8$ in figure 8(c). This is explained by the regions of positive and negative w' seen in figure 7(c) at the same wall-normal position. The streamwise correlations in figure 8(b, d) indicate that the correlation lengths on the unstable side of the channel are rather short in this direction. This supports the indications of non-steady vortices. It can also be noted that the most dramatic behaviour is seen on the stable side of the channel where the residues of the damped turbulence consist of essentially elongated structures.

The flow structures seen in figure 7 show similarities with Dean-type vortices (and similar to Taylor–Görtler vortices) observed in earlier studies by, e.g., Johnston *et al.* (1972) and Kristoffersen & Andersson (1993). The structures are, however, not stationary in time or in space although the time scale is rather large. While keeping in mind that the present study involves a different set of rotation numbers, it should be noted that the total sampling time in this investigation is significantly longer than that in the study by Kristoffersen & Andersson (1993).

5. Flow statistics

The turbulence statistics are collected from typically fifteen to twenty computational fields where each field is separated by a time period of $\sim 5.5\delta/u_\tau$. The averaging is done in space in the homogeneous directions by considering (x, z)-planes corresponding to

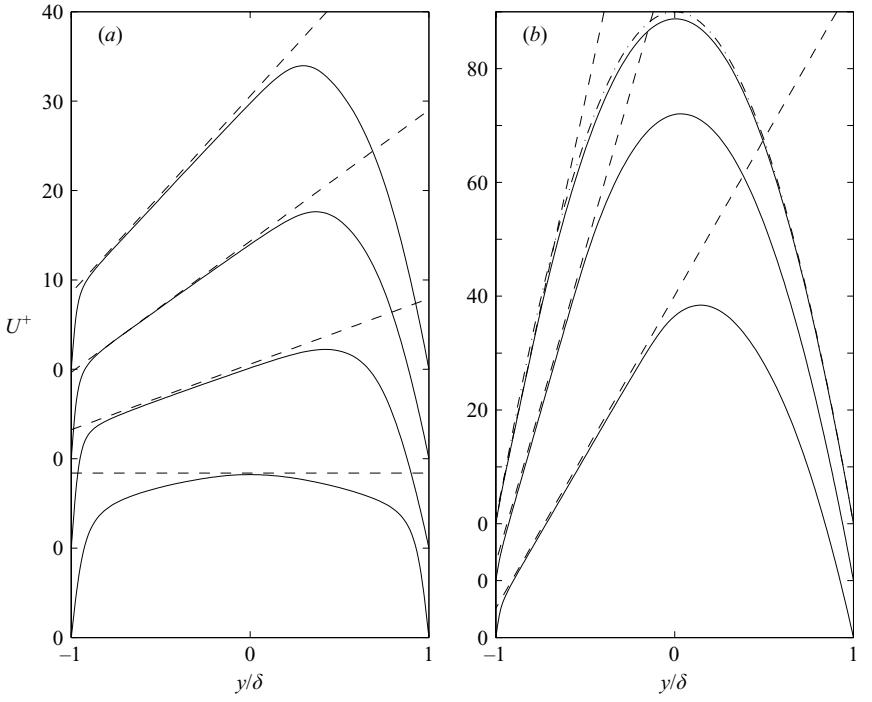

FIGURE 9. Mean velocity profiles, U^+, (*a*) for $Ro = 0$, 0.43, 0.77 and 0.98 (—) and (*b*) for $Ro = 1.50$, 2.06, 2.49 (—) and 3.0 (–·–). - - -, 2Ω-slope lines.

the same y-coordinate from all the fields. The flow is driven by a constant pressure gradient and hence Re_τ should attain (or be very close to) the *a priori* set value of 180. Table 1 presents the Reynolds and rotation numbers obtained in the present simulations.

5.1. *Mean flow*

The mean velocity profiles for $Ro = 0$ to 2.49 are shown in figure 9. For comparison, the mean velocity profiles from the simulations by Alvelius (1999) for $Ro = 0$, 0.43 and 0.77 are plotted in the same figure. The corresponding laminar profile has been plotted on the same level as that of $Ro = 2.49$, for comparison (dash-dotted curve). The laminar profile, as expected, matches the profile for the $Ro = 3.0$ case.

As can be seen, the slope of the mean velocity profile is very close to twice the system rotation rate ($\mathrm{d}U/\mathrm{d}y \approx 2\Omega$) for all turbulent cases. The extent of this region does, however, vary. For low rotation numbers, the study by Alvelius (1999) shows that this region increases its extent for increasing rotation numbers. For high rotation numbers it is clear from the present study that the 2Ω-slope region (for high enough Ro) decreases in extent for increasing rotation numbers.

The damping of the turbulence due to the increased system rotation gives an increased mean bulk flow, U_b^+. This is demonstrated in figure 10(*a*) in which the normalized bulk velocity $U_b^+ = U_b/u_\tau$ is plotted against the rotation number. The simulation results are marked with circles and the solid line is plotted in order to clarify the trend. Note that $U_b^+ = 60$ in figure 10(*a*) corresponds to the laminar bulk flow with $Re_\tau = 180$.

The rotation also affects the wall-shear velocities on the stable and unstable sides of the channel, as is shown in table 1. This is also depicted in figure 10(*b*) where

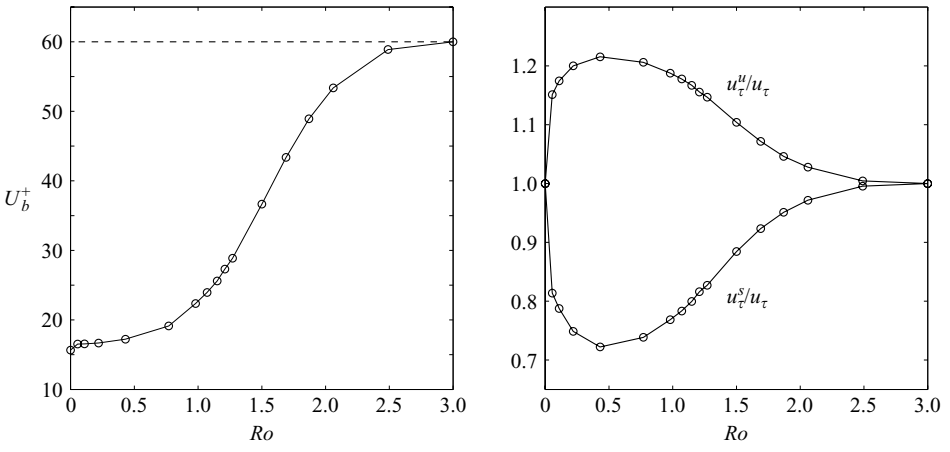

FIGURE 10. (*a*) Normalized bulk velocity, U_b^+, for different rotation numbers. DNS (○) and laminar U_b^+ (——). (*b*) Ratios u_τ^u/u_τ and u_τ^s/u_τ for different rotation numbers.

the ratios u_τ^s/u_τ and u_τ^u/u_τ are plotted against Ro. The data for the lower rotation numbers ($Ro \leqslant 0.77$) are taken from Alvelius (1999). The results presented here agree well with those of Kristoffersen & Andersson (1993). It can be noted that the largest difference in the wall-shear velocities on the unstable and stable sides should be obtained for a rotation number around 0.5. After this threshold rotation number the difference between the two sides decreases with increasing rotation number. For $Ro = 3.0$, in the present study, the flow has become laminar due to complete damping of the turbulence and the difference between u_τ^s and u_τ^u has vanished.

The higher u_τ^u for the rotating cases compared to the non-rotating cases gives a reduction of resolution. In the present study, the highest u_τ^u is obtained for $Ro = 0.98$. This corresponds to a resolution decrease, in wall units, by a factor of 1.19 on the unstable side of the channel compared to the non-rotating case. This should still be within tolerable limits.

5.2. *Reynolds stresses*

The normalized Reynolds stresses $\overline{u'v'}^+$ and the diagonal components $\overline{u'u'}^+$, $\overline{v'v'}^+$ and $\overline{w'w'}^+$ are shown in figure 11. The corresponding components from the simulations by Alvelius (1999) are also plotted for $Ro = 0$, 0.43 and 0.77. $Ro = 0.43$ is interesting from the point of view that it is closest (of the rotations studied by Alvelius 1999) to the rotation number for which the trend of decreasing $\overline{u'v'}^+$ is broken. It is also the rotation number that corresponds to the largest difference between u_τ^u and u_τ^s in figure 10(*b*). In the same simulations, $Ro = 0.77$ is the largest rotation number studied. $Ro = 0$ is included for comparison.

The rotation strongly affects the Reynolds stresses since it enters explicitly in the governing equations. Even the effect of small rotation rates is dramatic as demonstrated in previous studies by e.g. Kristoffersen & Andersson (1993) and Alvelius (1999), and the $\overline{u'v'}^+$-profile deviates significantly from the non-rotating case.

As the rotation rate is increased the magnitude of $\overline{u'v'}^+$ decreases, as shown in figure 11. It should be noted that in the region $-0.8 \leqslant y/\delta \leqslant 0$, the $\overline{u'v'}^+$-profiles for $Ro = 0$ and $Ro = 1.50$ are remarkably close to each other. Closer to the wall, however, the difference is much larger and the slope of the $\overline{u'v'}^+$-profile is significantly steeper

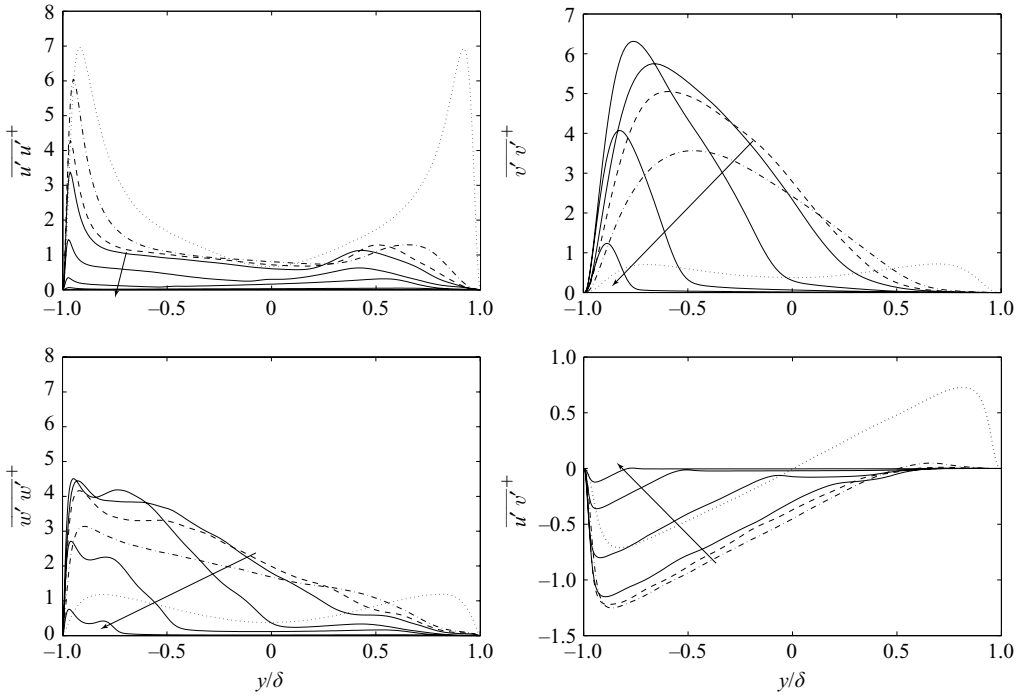

FIGURE 11. Reynolds stresses for $Re_\tau = 180$ and $Ro = 0.98$, 1.50, 2.06 and 2.49 (solid lines). Direction of arrow indicates increasing rotation number. Also shown are $Ro = 0$ ($\cdots$), $Ro = 0.43$ ($-\cdot$) and $Ro = 0.77$ ($--$) from Alvelius (1999).

for the rotating cases. As a result the wall-shear velocity attains larger values on the unstable side.

Note the 'second plateau' of the $\overline{u'v'}^+$-profile. Here, $y/\delta \sim 0.25$, the Reynolds shear stress is negative while the slope of the velocity profile changes sign. This implies a negative production in the part of this region where the mean velocity profile has a negative slope. Closer to the wall on the stable side, the $\overline{u'v'}^+$-levels are very small as can be seen in figure 11.

The normal components of the Reynolds stress tensor are plotted in figure 11. For the rotation numbers studied, the increased rotation rate has an overall damping effect on the normal components. This effect is however stronger in the centre of the channel than close to the wall. $\overline{u'u'}^+$ is an exception from this with a strong influence of the rotation on the peak close to the wall on the unstable side. In fact, for the higher rotation numbers the $\overline{u'u'}$-component, which is completely dominating for the non-rotating case, gives the smallest contribution to the total turbulence kinetic energy. It should also be noted that the wall-normal velocity fluctations are small for the major part of the stable side. This is increasingly evident with increasing rotation number and is of course a result of the trend seen in figure 6. The other normal components are relatively small, but still significant in this region, corresponding to the structures seen in figure 5.

The normalized turbulence dissipation rate is shown in figure 12. In contrast to all Reynolds stresses (except $\overline{u'u'}^+$) the behaviour of ε^+ is monotonic on the unstable side of the channel and increasing with increasing rotation for rotation numbers up to

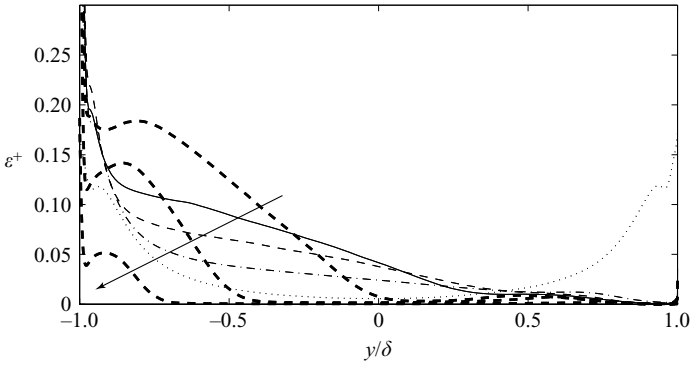

FIGURE 12. Normalized dissipation rate, ε^+, for $Ro = 0.98$ (—) and $Ro = 1.50$, 2.06 and 2.49 (thick dashed lines). Direction of arrow indicates increasing rotation number for $Ro \geqslant 1.50$. Also shown, $Ro = 0$ (···), $Ro = 0.43$ (—·) and $Ro = 0.77$ (——) from Alvelius (1999).

$Ro = 1.50$ (of the shown Ro). For higher rotation numbers, an increased damping for increasing rotation numbers can be seen. On the stable side, the dissipation rates are low and comparable for all rotations numbers in the present study. It is interesting, however, that for all the rotating cases the dissipation is very close to zero at the wall on the suction side.

6. Balance of the Reynolds stress transport equation

In order to illustrate the influence of the different physical phenomena on the statistics, the different terms of the Reynolds stress transport equation are plotted in figure 13 for $Re_\tau = 180$ and $Ro = 1.50$. For this rotation number, the largest magnitudes can be observed on the unstable side of the channel where the turbulence is produced. While the production feeds only the $\overline{u'u'}^+$ and $\overline{u'v'}^+$ components, the Coriolis term redistributes energy into the $\overline{v'v'}^+$ component and is balanced by, essentially, the dissipation and the pressure–strain. The pressure–strain, on the other hand transfers energy from the $\overline{v'v'}^+$-component back into the $\overline{u'u'}^+$- and especially the $\overline{w'w'}^+$-components. This is the only mechanism for feeding energy into the $\overline{w'w'}^+$-component. One can observe that the diffusion is small for all components except $\overline{v'v'}^+$ for which, however, the triple and pressure parts of the diffusion balance each other in a large region of the unstable side. The dissipation is significant only for the $\overline{v'v'}^+$- and $\overline{w'w'}^+$-components.

The negative production of turbulence kinetic energy due to negative $\overline{u'v'}^+$ and negative slope of the mean velocity profile in a region to the right of where $\mathrm{d}U/\mathrm{d}y = 0$ can be seen in figure 13 through $\mathscr{P}_{11}$. In terms of flow physics a negative production means an inversed energy cascade, i.e. energy is taken from the turbulence and fed into the mean flow. This is an interesting effect that is seldom encountered. Since energy is fed to the total turbulence kinetic only through $\mathscr{P}_{11}$, a negative $\mathscr{P}_{11}$ on the stable side must imply that there is a mechanism that transports turbulence into this region. In order to study this phenomenon in more detail figure 14 presents plots of the region $-0.2 \leqslant y/\delta \leqslant 1.0$ for the $\overline{u'u'}^+$-, $\overline{v'v'}^+$- and $\overline{u'v'}^+$-components. As can be seen, the transport of turbulence kinetic energy into the stable side of the channel probably occurs through the pressure correlation part of the diffusion, G_{ij}, for the

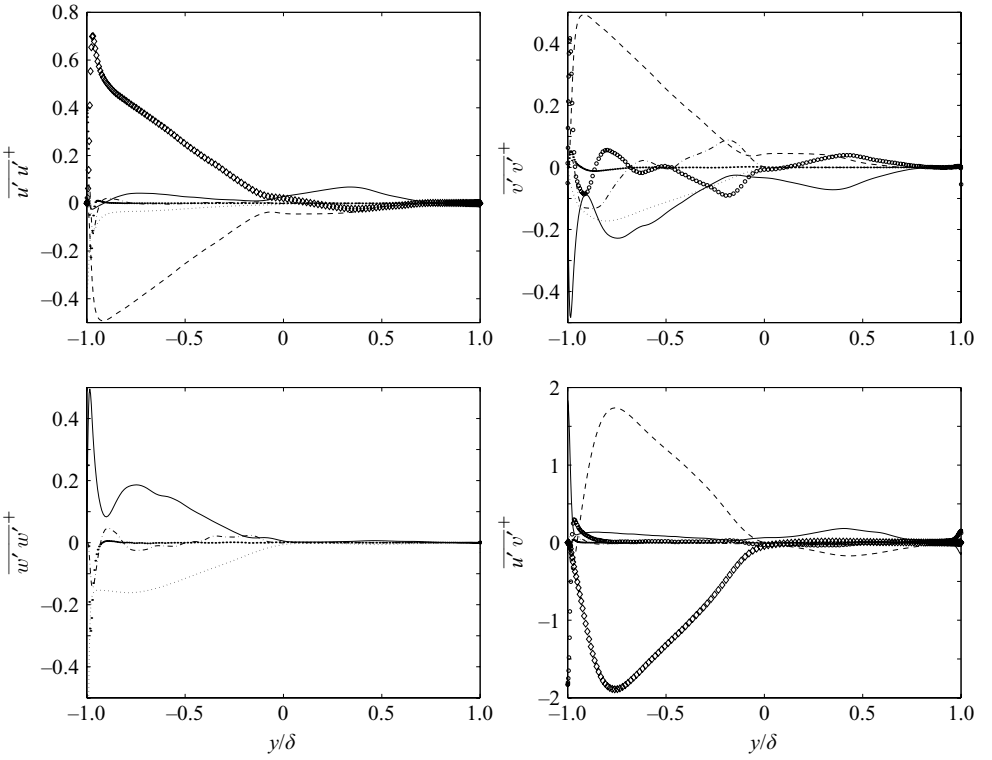

FIGURE 13. The terms of the transport equation of the Reynolds stresses for $Re_\tau = 180$ and $Ro = 1.50$: $\mathscr{P}_{ij}^+$ ($\diamond$), C_{ij}^+ (——), Π_{ij}^+ (-), $-\varepsilon_{ij}^+$ ($\cdots$), $-\mathscr{T}_{ij}^+$ (–·), $\mathscr{D}_{ij}^{v+}$ (●) and $-G_{ij}^+$ (○).

$\overline{v'v'}^+$-component. A closer investigation of the $\overline{u'u'}^+$-component of figure 14 reveals, however, that there is a region $y/\delta \sim 0.8$ where $P_{11} > 0$. In comparison to G_{22}, $\mathscr{P}_{11}$ can still be regarded as insignificant. Furthermore, the small peak of $\overline{u'u'}^+$ on the stable side of the channel seen in figure 11, approximately coincides with the peaks of the redistribution terms and G_{22} in figure 14. The presence of turbulence in this region should therefore be ascribed to the diffusion of $\overline{v'v'}^+$ through G_{22}.

The diffused wall-normal velocity fluctuations are redistributed, through the pressure–strain correlation, to the $\overline{u'u'}^+$-component which despite negative production and a damping Coriolis term, attains a significant magnitude on the stable side. From this point of view, the effects of pressure–strain and Coriolis forces should be seen as one single redistributing mechanism. The non-zero $\overline{u'u'}^+$, which is larger than $\overline{v'v'}^+$ in this region, then implies that the Coriolis term, $C_{12} = 2\Omega(\overline{v'v'}^+ - \overline{u'u'}^+)$, forces $\overline{u'v'}^+$ to be negative. This effect is slightly amplified by the pressure part of the diffusion, G_{12}. Balance of the $\overline{u'v'}^+$-equation, in this region, is obtained through the pressure–strain which seems to attain the appropriate magnitude more passively. For this particular flow case, a negative production hence relies strongly on the diffusion of wall-normal velocity fluctuations to the stable side of the channel and that at least a part of this energy is redistributed to the streamwise velocity fluctuations.

Hence, the elongated flow structures seen on the stable side of the channel in figures 4 and 5 are sustained by the forcing from the unstable side. From a statistical

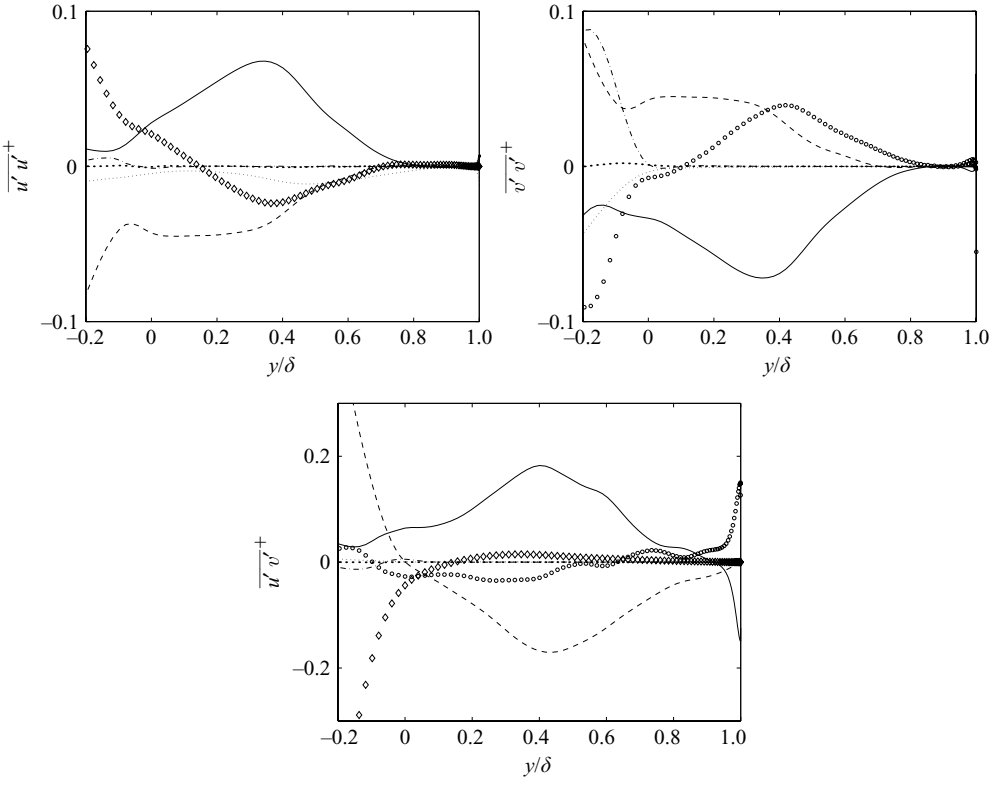

FIGURE 14. The terms of the transport equation of the Reynolds stresses for $Re_\tau = 180$ and $Ro = 1.50$: $\mathscr{P}_{ij}^+$ ($\diamond$), C_{ij}^+ (——), Π_{ij}^+ (—), $-\varepsilon_{ij}^+$ ($\cdots$), $-\mathscr{T}_{ij}^+$ (—·), $\mathscr{D}_{ij}^{\nu+}$ (●) and $-G_{ij}^+$ (○).

perspective, this mechanism corresponds to the diffusion of wall-normal stress, $\overline{vv}$, from the unstable side into the stable side of the channel.

7. Discussion

For all turbulent simulations in the present investigation, the classical features of e.g. a mean velocity slope of approximately twice the system rotation rate in the centre of the channel and an increasingly more laminar-like stable sides observed in previous studies, see e.g. Kristoffersen & Andersson (1993) and Alvelius (1999), are confirmed. The trend of decreasing difference between the wall-shear velocities of the stable and unstable sides with increasing rotation number for high enough rotation numbers, suggested by Alvelius (1999), is also confirmed. The extent of the low-turbulence region on the stable side increases with increasing rotation rate and the overall turbulence level decreases. Eventually the flow laminarizes completely and the velocity profile is given by a (symmetric) parabola. Among the rotation numbers studied, complete flow laminarization occurs at $Ro = 3.0$ for which the initially added disturbances are damped out.

The numerical simulation for each rotation rate was initiated with the turbulent solution from the preceding lower rotation rate. Moreover, the case $Ro = 2.06$ was also initiated with a laminar field with a superimposed disturbance which evolved to the same statistical solution as when initiated with the turbulent solution. The $Ro = 3.0$ case was, however, only initiated with a laminar field with a superimposed

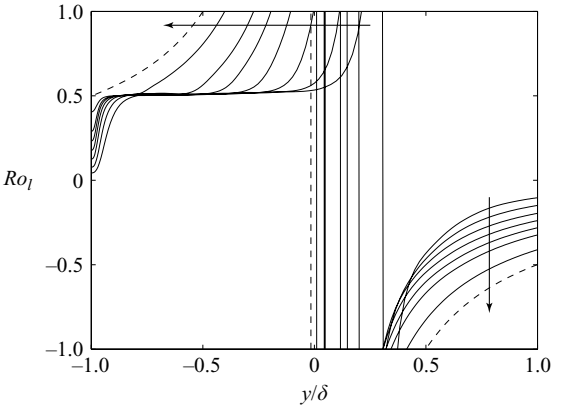

FIGURE 15. Local rotation number, $Ro_l = \Omega/(\mathrm{d}U/\mathrm{d}y)$, for $Ro = 0.98$, 1.27, 1.50, 1.69, 1.87, 2.06 and 2.49. The arrow indicates increasing rotation number. Laminar flow (——), $Ro = 3.0$.

disturbance. Laminarization of a turbulent state is, thus, not completely proven but the monotonic decay of turbulence during the successive increase of rotation rate up to $Ro = 2.49$ and the repeatability of one of the highest rotation rates from different initial states are strong indications that the flow will laminarize at or below $Ro = 3.0$.

The limiting behaviour at the laminar state can also be analysed by considering linear stability. A rotating shear flow is linearly stable if the parameter $B = 2Ro_l(2Ro_l - 1)$, introduced by Bradshaw (1969), is positive and $Ro_l = \Omega/(\mathrm{d}U/\mathrm{d}y)$. For a parabolic laminar velocity profile, B will be negative everywhere for $Ro > 3.0$, and, thus, the flow cannot undergo transition to turbulence until $Ro < 3.0$. Whether turbulence can be sustained for $Ro > 3.0$ cannot, however, be predicted from linear stability theory. Stability might be preserved by viscous effects even for lower rotation numbers. It should be pointed out that for $Ro = 3.0$, the absolute value of the mean velocity slope at the wall of either side of the channel is equal to 2Ω.

Interesting comparisons can be made with rotating homogeneous turbulent flow regarding the laminarization of rotating turbulent channel flow. For this purpose it is useful to consider Ro_l as the local rotation number. According to the analysis of rotating homogeneous shear flow made by various authors, see e.g. Salhi & Cambon (1997) and Brethouwer (2005), neutral stability is achieved for $Ro_l = 0.5$ while $Ro_l > 0.5$ should have a damping effect on the turbulence. For negative Ro_l, Brethouwer (2005) demonstrated that $Ro_l = -0.25$ leads to decaying turbulence in rotating homogeneous shear flow. Rotating turbulent channel flow is affected by the same mechanisms and in order to see the similarities more clearly, Ro_l of the present simulations is plotted for different rotation numbers in figure 15. The region where $Ro_l = 0.5$ simply corresponds to the 2Ω slope of the mean velocity profile. Note also that when $\mathrm{d}U/\mathrm{d}y$ changes sign, Ro_l does too. The analogy with rotating homogeneous shear flow indicates that, for the higher rotation numbers, disturbances can grow in a narrow band close to the wall on the unstable side only. It is also clear that the $Ro = 3.0$ case is outside the 'growth region' in the whole domain. Turbulence can hence be expected to decay, implying a laminar flow, which apparently also happens. The region where $Ro_l \sim 0.5$ also seems to be strongly connected to the part of the domain where significant wall-normal velocity fluctuations can be found. By analysing the DNS data one can further observe that the peak of the production of turbulence kinetic energy on the unstable side of the channel is very close to where

$Ro_l = 0.25$. There are, thus, indications from both homogeneous shear flow as well as from the present DNS of rotating channel flow that the linear stability argument is also applicable in turbulent flow around the $Ro_l = 0.5$ neutral stability limit. If this is the case, the 2Ω slope can be explained. If the mean velocity profile is perturbed from the 2Ω slope the turbulence will be amplified or damped such that the mean flow will be driven back to the 2Ω slope. This mechanism has been demonstrated by Tanaka *et al.* (2000) for a laminar mean velocity profile with superimposed large (nonlinear) perturbations. Hamba (2006) used modelling concepts, including non-local effects, to study the mechanism underlying the zero mean absolute vorticity state in rotating channel flow, i.e. the tendency to establish the 2Ω slope.

It is important to emphasize that channel flow is affected by phenomena not present in homogenous shear flow. Diffusive transport of Reynolds stress components, for instance, is probably an essential mechanism for maintaining turbulence in the part of the domain where Ro_l is not favourable. Furthermore, as pointed out in the preceeding section, there is a small production on the stable side close to the wall. This is true for all turbulent rotation numbers in the present study, even for $Ro_l < -0.25$ at the wall on the stable side, and is a result of having a very low, but still high enough, correlation between the streamwise and wall-normal velocity fluctuations in this region. From this point of view the velocity fluctuations are not completely damped out on the stable side as one might believe by looking at figure 11. It seems, however, that a necessary condition for obtaining a turbulent flow at all is to have an adequately low/high Ro_l in some region.

The present investigation is for a rather restricted Reynolds number of $Re_\tau = 180$. For low Reynolds numbers the flow will be damped by viscous effects, so there is very probably a Reynolds number dependence on the rotation number for which the flow laminarizes. We expect, however, that the indications of laminarization of rotating turbulent channel flow at $Ro = 3.0$ are so strong that this limit can be seen as a universal upper limit for which this flow must be laminarized for all Reynolds numbers. This will be addressed in future studies.

The authors gratefully acknowledge the use of simulation data obtained by Krister Alvelius, see Alvelius (1999), for comparison with data obtained in the present simulations.

REFERENCES

Alvelius, K. 1999 Studies of turbulence and its modelling through large eddy- and direct numerical simulation. PhD thesis, Department of mechanics, KTH, Stockholm, Sweden.

Bech, K. H. & Andersson, H. I. 1997 Turbulent plane couette flow subject to strong system rotation. *J. Fluid Mech.* **347**, 289–318.

Bradshaw, P. 1969 The analogy between streamline curvature and buoyancy in turbulent shear flow. *J. Fluid Mech.* **36**, 177–191.

Brethouwer, G. 2005 The effect of rotation on rapidly sheared homogeneous turbulence and passive scalar transport. linear theory and direct numerical simulation. *J. Fluid Mech.* **542**, 305–342.

Hamba, F. 2006 The mechanism of zero mean absolute vorticity state in rotating channel flow. *Phys. Fluids* **18**.

Henningson, D. S., Lundbladh, A. & Johansson, A. V. 1993 A mechanism for bypass transition from localized disturbances in wall-bounded shear flows. *J. Fluid Mech.* **250**, 169–207.

Johnston, J. P., Halleen, R. M. & Lezius, D. K. 1972 Effects of spanwise rotation on the structure of two-dimensional fully developed turbulent channel flow. *J. Fluid Mech.* **56**, 533–559.

Kim, J., Moin, P. & Moser, R. 1987 Turbulence statistics in fully developed channel flow at low Reynolds number. *J. Fluid Mech.* **177**, 133–166.

Kristoffersen, R. & Andersson, H. I. 1993 Direct simulations of low-Reynolds-number turbulent flow in a rotating channel. *J. Fluid Mech.* **256**, 163–197.

Lamballais, E., Lesieur, M. & Métais, O. 1996 Effects of spanwise rotation on the vorticity stretching in transitional and turbulent channel flow. *Intl J. Heat Fluid Flow* **17**, 324–332.

Lamballais, E., Métais, O. & Lesieur, M. 1998 Spectral-dynamic model for large-eddy simulations of turbulent rotating channel flow. *Theor. Comp. Fluid Dyn.* **12**, 146–177.

Lesieur, M., Métais, O. & Comte, P. 2005 *Large-eddy Simulations of Turbulence*. Cambridge University Press.

Lundblad, A., Henningson, D. S. & Johansson, A. V. 1992 An efficient spectral integration method for the solution of the Navier-Stokes equations. *Tech. Rep.* FOI, FFA, SE-16490 Stockholm, Sweden, 1992-28.

Maciel, Y., Picard, D., Yan, G. & Dumas, G. 2003 Fully developed turbulent channel flow subject to system rotation. *AIAA Paper* 2003-4153.

Nagano, Y. & Hattori, H. 2003 Direct numerical simulation and modelling of spanwise rotating channel flow with heat transfer. *J. Turbulence* **4**.

Nakabayashi, K. & Kitoh, O. 1996 Low Reynolds number fully developed two-dimensional turbulent channel flow with system rotation. *J. Fluid Mech.* **315**, 1–29.

Nakabayashi, K. & Kitoh, O. 2005 Turbulence characteristics of two-dimensional channel flow with system rotation. *J. Fluid Mech.* **528**, 355–377.

Oberlack, M. 2001 A unified approach for symmetries in plane parallel turbulent shear flows. *J. Fluid Mech.* **427**, 299–328.

Salhi, A. & Cambon, C. 1997 An analysis of rotating shear flow using linear theory and dns and les results. *J. Fluid Mech.* **347**, 171–195.

Tanaka, M., Kida, S., Yanase, S. & Kawahara, G. 2000 Zero-absolute-vorticity state in a rotating turbulent shear flow. *Phys. Fluids* **12**, 1979–1985.

Wu, H. & Kasagi, N. 2004 Effects of arbitrary directional system rotation on turbulent channel flow. *Phys. Fluids* **16**, 979–990.